Fast Hardware Approach to Determining Mutual Coupling of Series–Series-Compensated Wireless Power Transfer Systems With Active Rectifiers

Yun Yang, *Member, IEEE*, Siew Chong Tan, *Senior Member, IEEE*, and Shu Yuen Ron Hui, *Fellow, IEEE*

***Abstract*—Maximum energy efficiency tracking of series–series-compensated wireless power transfer systems with active rectifiers require the information of mutual coupling coefficient or correlated variables, which are conventionally monitored based on the feedback signals from the receivers to the transmitters via a wireless communication system. In this article, a very fast hardware-based front-end monitoring strategy is proposed to determine the mutual coupling coefficient of the system within typically 62 ms without any wireless communication system. Compared to existing mathematical model-based methods, the proposed strategy is much faster and more cost-effective by using fewer sensors and simpler equations. The proposed method can therefore be implemented in low-cost digital controllers. Importantly, the parameter values of the transmitter and receiver resonators are not required by the proposed method. Both simulation and experimental results are included to validate the high accuracy and fast speed of the proposed monitoring strategy to monitor the coupling coefficient. Comparative results among the proposed and existing monitoring strategies are also presented.**

***Index Terms*—Coupling coefficient, front-end monitoring, series–series (SS)-compensated wireless power transfer (WPT).**

I. Introduction

RECENT advancements of series–series (SS)-compensated wireless power transfer (WPT) technology have enabled its wide-spread applications in battery charging of portable devices, electric vehicles (EV), and medical implants [1]. A conventional SS-compensated WPT system consists of an inverter at the transmitter side to maximize the overall system efficiency typically by phase control or frequency control, and a dc–dc converter at the receiver side to regulate the charging current and voltage of the battery load [2]–[7]. However, the efficiency and dynamic response of the conventional WPT system is limited by the dc–dc converter in point-of-load applications [8]. Alternatively, WPT systems with active rectifiers can address these issues and additionally avoid discontinuous operation of the diode-bridge rectifier, reduce system complexity, and improve power density [9]–[16]. The concept of maximum energy efficiency tracking (MEET) was first proposed in [2], which sparked off more related studies in [3], [4], [6], [7], [11], [12], and [16]. Fast control strategies for MEET strategies are subsequently investigated in [9], [14], and [16]. These fast MEET strategies normally require feedback signals from the receiver to the transmitter via a wireless communication system to calculate the coupling coefficient or correlated variables. The additional wireless communication system increases the volume and cost of the system.

Recently proposed front-end (primary-side) monitoring strategies can address this issue by monitoring the mutual coupling coefficient of SS-compensated WPT systems without an extra wireless communication system [17]–[21]. These strategies are designed based on the equivalent circuit models of the WPT systems. In [17], a switched capacitor is added at the transmitter side to enable the WPT system to operate in two modes. A mathematical model is established according to the two operating modes for coupling coefficient monitoring of the WPT system. The main advantage of this strategy is the capability of monitoring WPT systems with resistive, inductive, or inductive–resistive loads. The drawback of this strategy is the switched capacitor, which increases the cost and complexity of the system, and changes the resonant frequency of the transmitter resonator. In [18], the coupling coefficient of an SS-compensated WPT system is uniquely determined by measuring the input voltage and current at only one frequency. Based on this method, an alternative strategy is designed to monitor the coupling coefficient at two different frequency points which are slightly higher than the resonant frequency [19]. Besides, a frequency-sweep-based monitoring strategy using a simpler estimation equation is proposed in [20]. Compared to the strategies in [18] and [19], the method of [20] can be easily implemented in inexpensive digital controllers. However, its accuracy deteriorates when the leakage inductances of the coils are not perfectly compensated. The three monitoring strategies can rapidly monitor the coupling coefficient of SS-compensated WPT systems with either

Manuscript received September 6, 2019; revised December 5, 2019; accepted January 21, 2020. Date of publication February 28, 2020; date of current version June 23, 2020. This work was supported in part by Hong Kong Research Grant Council under Grant GRF 17203517 and in part by the University of Hong Kong (the U.S. provisional patent application 62/906,180, Sep. 26, 2019). Recommended for publication by Associate Editor M. Vitelli. *(Corresponding author: Shu Yuen Ron Hui.)*

Yun Yang and Siew Chong Tan are with the Department of Electrical and Electronic Engineering, The University of Hong Kong, Hong Kong (e-mail: cacalotoyangyun@gmail.com; sctan@eee.hku.hk).

Shu Yuen Ron Hui is with the Department of Electrical and Electronic Engineering, The University of Hong Kong, Hong Kong, and also with the Department of Electrical and Electronic Engineering, Imperial College London, London SW7 2AZ, U.K. (e-mail: ronhui@eee.hku.hk).

Color versions of one or more of the figures in this article are available online at http://ieeexplore.ieee.org.

Digital Object Identifier 10.1109/TPEL.2020.2977140

TABLE I
FEATURES OF THE MONITORING STRATEGIES

Feature	[17]	[18]	[19]	[20]	[21]	Proposed
High accuracy for unknown parameters of the resonators	×	×	×	×	√	√
Easy implementation using inexpensive digital controllers	×	×	×	√	×	√
Fast monitoring	√	√	√	√	×	√
Numbers of sensors	2	2	2	2	2	1

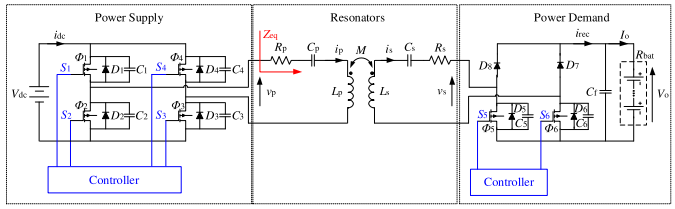

Fig. 1. Circuitry of an SS-compensated WPT system with a semi-bridgeless rectifier.

passive or active rectifiers. Nevertheless, these strategies are only validated for WPT systems with pure-resistive loads. Besides, the accuracies of these monitoring strategies are affected by some parameters of the resonators, which highly depend on the operating conditions of WPT systems. For instance, the sensitivity of the monitored mutual inductance with respect to the equivalent series resistance (ESR) of the primary coil is low for the WPT system operating at around 250 kHz. However, such sensitivity is quite high for the WPT system operating at around 100 kHz. Considering the advantages and drawbacks, the strategies in [18] and [19] are more suitable for wireless battery charging systems with fixed parameters and requirements for accurate system monitoring, e.g., medical implants. The strategy in [20] is more suitable for wireless battery charging systems with fixed parameters and high compactness, e.g., portable devices. To overcome the issues of the strategies in [18]–[20], heuristic algorithms are used to monitor the coupling coefficient of SS-compensated WPT systems without knowing the exact parameter values of the resonators and can be extended to monitor the WPT systems with inductive, inductive–resistive, or capacitive loads [21]. However, this monitoring strategy is computationally intensive and therefore cannot be used for fast and online monitoring. This strategy is more suitable for stationary WPT systems having high-performance computation resources at transmitter sides, e.g., stationary wireless EV charging systems. These "model-based" methods for determining the mutual coupling coefficient require mathematical calculations based on fundamental equivalent circuits of WPT systems and thus their performance also depends on the computational speed of the controllers.

In this article, a very fast "hardware-based" strategy is proposed to accurately and rapidly monitor the mutual coupling coefficients of SS-compensated WPT systems. The estimation of the mutual coupling coefficient can be achieved by shorting the rectifier outputs to ground momentarily. The motivation of this investigation is to eliminate the disadvantages of the existing model-based monitoring strategies in [17]–[21] without the need for a wireless communication system for feedback control. The instructions of shorting the rectifier outputs to ground from transmitters to receivers can be implemented using frequency shift keying, which is a well-established technique for Qi-compliant devices [22].

The major comparisons among the existing monitoring strategies and the proposed monitoring strategy are comprehensively shown in Table I. For the existing model-based monitoring strategies, both the fundamental components of the input voltage of the transmitting resonator and the transmitter current are required to be accurately measured for obtaining their amplitude/root-mean-square values. Therefore, both voltage and current sensors are needed. For the proposed hardware-based monitoring strategy, only the phase difference between the switching signal of the inverter and the transmitter current is required. Hence, only one current sensor is needed. Besides, the simple estimation equations of the proposed monitoring strategy are only dependent on the resonant and operating frequencies. Consequently, the proposed monitoring strategy can achieve fast monitoring of the coupling coefficient using inexpensive digital controllers and guarantee high accuracy even for systems with unknown parameter values of the resonators. Furthermore, because the estimation process is carried out by short-circuiting the outputs of the active rectifiers (i.e., independent of the load type), the proposed monitoring strategy can be used for WPT systems with various types of loads.

II. ANALYSIS AND DESIGN OF THE PROPOSED MONITORING STRATEGY

To simplify the analysis without a loss of generality, an SS-compensated WPT system with a semi-bridgeless (S-BAR) rectifier is investigated in this article. WPT systems using S-BAR is not new. A voltage control scheme for WPT systems with S-BAR has been reported in [23]. Our proposal applies to any receiver circuit with the possibility of shorting the rectifier output terminals.

The circuitry of the system is depicted in Fig. 1. The transmitter circuit consists of a power inverter driving a transmitter resonator that comprises a transmitter coil, i.e., $L_{\rm p}$ and a series-compensated capacitor, i.e., $C_{\rm p}$. The stray resistance in $L_{\rm p}$ and $C_{\rm p}$ is represented as $R_{\rm p}$. The power inverter generates an ac rectangular voltage across the transmitter resonator. The receiver circuit consists of a receiver coil, i.e., $L_{\rm s}$ and series-compensated capacitor, i.e., $C_{\rm s}$, with $L_{\rm s}$ and $C_{\rm s}$ forming the receiver resonator. The stray resistance of this receiver resonator is represented as $R_{\rm s}$. The receiver resonator feeds the S-BAR rectifier, which is connected directly to the battery load without using any battery management circuits.

In the proposed strategy, the determination of the mutual coupling coefficient requires the short-circuiting of the rectifier output momentarily for a short period typically less than 62 ms. For the system in Fig. 1, the switches Φ_5 and Φ_6 are closed in the active rectifier for this purpose. The equivalent circuit of the system during the monitoring stage is shown in Fig. 2. Based on fundamental voltage analysis, the AC rectangular voltage

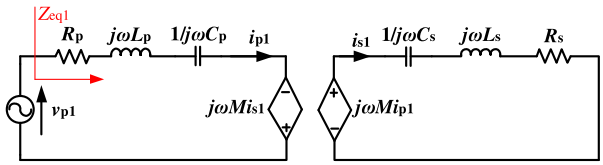

Fig. 2. Equivalent circuit of the SS-compensated WPT system when both switches of the S-BAR rectifier are closed.

generated by the power inverter can be approximated as a sinusoidal voltage $v_{\rm p1}$. The fundamental components of the transmitter current and the receiver current of the receiver resonator are $i_{\rm p1}$ and $i_{\rm s1}$, respectively, ω is the switching angular frequency, and M is the mutual inductance between the transmitter and receiver coils. The coupling coefficient (i.e., k) of the SS-compensated WPT system is as follows:

$$k = \frac{M}{\sqrt{L_{\rm p}L_s}}. \tag{1}$$

Based on the equivalent circuit in Fig. 2

$$\begin{cases} v_{\rm p1} = Z_{\rm p1} i_{\rm p1} - j\omega M i_{\rm s1} \\ 0 = Z_{\rm s1} i_{\rm s1} - j\omega M i_{\rm p1} \end{cases} \tag{2}$$

where $Z_{\rm p1} = j\omega L_{\rm p} + \frac{1}{j\omega C_{\rm p}} + R_{\rm p}$ and $Z_{\rm s1} = j\omega L_s + \frac{1}{j\omega C_s} + R_s$. $C_{\rm p}$ and $C_{\rm s}$ are, respectively, designed to compensate $L_{\rm p}$ and $L_{\rm s}$

$$\omega_{\rm op}^2 = \frac{1}{L_{\rm p}C_{\rm p}} \tag{3.1}$$

$$\omega_{\rm os}^2 = \frac{1}{L_s C_s} \tag{3.2}$$

where $\omega_{\rm op}$ and $\omega_{\rm os}$ are the resonant angular frequencies of the transmitter and the receiver, respectively. By substituting (3) into (2) and simplifying (2) by cancelling $i_{\rm s1}$, we get

$$Z_{\rm eq1} = \frac{v_{\rm p1}}{i_{\rm p1}} = Z_{\rm p1} + \frac{\omega^2 M^2}{Z_{\rm s1}} = R_{\rm eq1} + jX_{\rm eq1} \tag{4.1}$$

where

$$R_{\rm eq1} = R_{\rm p} + \frac{\omega^2 M^2}{R_s + \frac{\left(1-\frac{\omega_{\rm os}^2}{\omega^2}\right)^2 \omega^2 L_s^2}{R_s}} > 0 \tag{4.2}$$

$$X_{\rm eq1} = \left(1 - \frac{\omega_{\rm op}^2}{\omega^2}\right)\omega L_{\rm p} - \frac{\left(1-\frac{\omega_{\rm os}^2}{\omega^2}\right)\frac{\omega M^2}{L_s}}{\left(1-\frac{\omega_{\rm os}^2}{\omega^2}\right)^2 + \frac{R_s^2}{\omega^2 L_s^2}}. \tag{4.3}$$

Generally, the receiving coil has a high-quality factor (i.e., $\frac{R_s^2}{\omega^2 L_s^2} \approx 0$). Then, (4.3) can be simplified as follows:

$$X_{\rm eq1} = \left(1 - \frac{\omega_{\rm op}^2}{\omega^2}\right)\omega L_{\rm p} - \frac{\frac{\omega M^2}{L_s}}{1-\frac{\omega_{\rm os}^2}{\omega^2}} \left(\omega \neq \omega_{\rm os}\right) \tag{4.4}$$

and

$$X_{\rm eq1} = \left(1 - \frac{\omega_{\rm op}^2}{\omega_{\rm os}^2}\right)\omega_{\rm os} L_{\rm p} \left(\omega = \omega_{\rm os}\right). \tag{4.5}$$

TABLE II
REACTANCE CHARACTERISTICS OF $X_{\rm eq1}$

	$\omega_{\rm op}<\omega_{\rm os}$			
	$\omega_{\rm op}<\omega_{\rm os}<\omega$	$\omega_{\rm op}<\omega<\omega_{\rm os}$	$\omega<\omega_{\rm op}<\omega_{\rm os}$	$\omega_{\rm op}<\omega_{\rm os}=\omega$
$k<k_{\rm c}$	inductive	nonexistent	capacitive	inductive
$k>k_{\rm c}$	capacitive	capacitive	inductive	inductive
$k=k_{\rm c}$	zero	nonexistent	zero	inductive
	$\omega_{\rm op}>\omega_{\rm os}$			
	$\omega_{\rm os}<\omega_{\rm op}<\omega$	$\omega_{\rm os}<\omega<\omega_{\rm op}$	$\omega<\omega_{\rm os}<\omega_{\rm op}$	$\omega=\omega_{\rm os}<\omega_{\rm op}$
$k<k_{\rm c}$	inductive	nonexistent	capacitive	capacitive
$k>k_{\rm c}$	capacitive	capacitive	inductive	capacitive
$k=k_{\rm c}$	zero	nonexistent	zero	capacitive
	$\omega_{\rm op}=\omega_{\rm os}=\omega_{\rm o}$			
	$\omega<\omega_{\rm o}$		$\omega>\omega_{\rm o}$	$\omega=\omega_{\rm o}$
$k<k_{\rm c}$	capacitive $(0<k\leq\frac{\omega_{\rm o}^2}{\omega^2}-1)$		inductive $(0<k\leq 1-\frac{\omega_{\rm o}^2}{\omega^2})$	zero
$k>k_{\rm c}$	inductive $(\frac{\omega_{\rm o}^2}{\omega^2}-1<k\leq 1)$		capacitive $(1-\frac{\omega_{\rm o}^2}{\omega^2}<k\leq 1)$	zero
$k=k_{\rm c}$	zero		zero	zero

By substituting (1) into (4.4)

$$X_{\rm eq1} = \omega L_{\rm p}\left[\left(1 - \frac{\omega_{\rm op}^2}{\omega^2}\right) - \frac{k^2}{1-\frac{\omega_{\rm os}^2}{\omega^2}}\right]\left(\omega \neq \omega_{\rm os}\right). \tag{4.6}$$

The reactance $X_{\rm eq1}$ can be inductive, capacitive, or zero for both (4.5) and (4.6). According to (4.5), if $\omega = \omega_{\rm os} > \omega_{\rm op}$, $X_{\rm eq1}$ is inductive for any k ($0\leq k\leq 1$); if $\omega = \omega_{\rm os} < \omega_{\rm op}$, $X_{\rm eq1}$ is capacitive for any k ($0\leq k\leq 1$); if $\omega = \omega_{\rm os} = \omega_{\rm op}$, $X_{\rm eq1}$ is zero for any k ($0\leq k\leq 1$). According to (4.6), if

$$\begin{cases} k^2 < k_c^2 & (\omega > \omega_{\rm os}) \\ k^2 > k_c^2 & (\omega < \omega_{\rm os}) \end{cases} \tag{5.1}$$

$X_{\rm eq1}$ is inductive if

$$\begin{cases} k^2 < k_c^2 & (\omega < \omega_{\rm os}) \\ k^2 > k_c^2 & (\omega > \omega_{\rm os}) \end{cases} \tag{5.2}$$

$X_{\rm eq1}$ is capacitive if

$$k^2 = k_c^2 \quad (\omega \neq \omega_{\rm os}) \tag{5.3}$$

$X_{\rm eq1}$ is zero, where $k_c = \sqrt{(1-\frac{\omega_{\rm op}^2}{\omega^2})(1-\frac{\omega_{\rm os}^2}{\omega^2})}$.

The reactance characteristics of $X_{\rm eq1}$ can be tabulated as shown in Table II. The coupling coefficient is in the range of $0 \leq k \leq 1$. Based on the reactance characteristics of $X_{\rm eq1}$ in Table II, the characteristics of the equivalent impedance $Z_{\rm eq1}$ in the k–ω plane for three possible cases of any SS-compensated WPT system with the receiving circuit being short-circuited are plotted in Fig. 3(a)–(c). When ω and k of the system are located in the inductive/capacitive zones (including inductive/capacitive line), $Z_{\rm eq1}$ is inductive/capacitive. When ω and k of the system are located on the zero lines, $Z_{\rm eq1}$ is purely resistive. The intersection points of any k with the zero lines form Point-*A* and Point-*B* for any compensation ($\omega_{\rm op} < \omega_{\rm os}$, $\omega_{\rm op} > \omega_{\rm os}$, or $\omega_{\rm op} = \omega_{\rm os}$). Point-*A* can be determined when ω of the WPT system is swept from the minimum $\omega_{\rm min}$ to the maximum $\omega_{\rm max}$. Point-*B* is determined when ω is swept from the maximum $\omega_{\rm max}$ to the minimum $\omega_{\rm min}$. Based on (5.3), the analytical expressions of

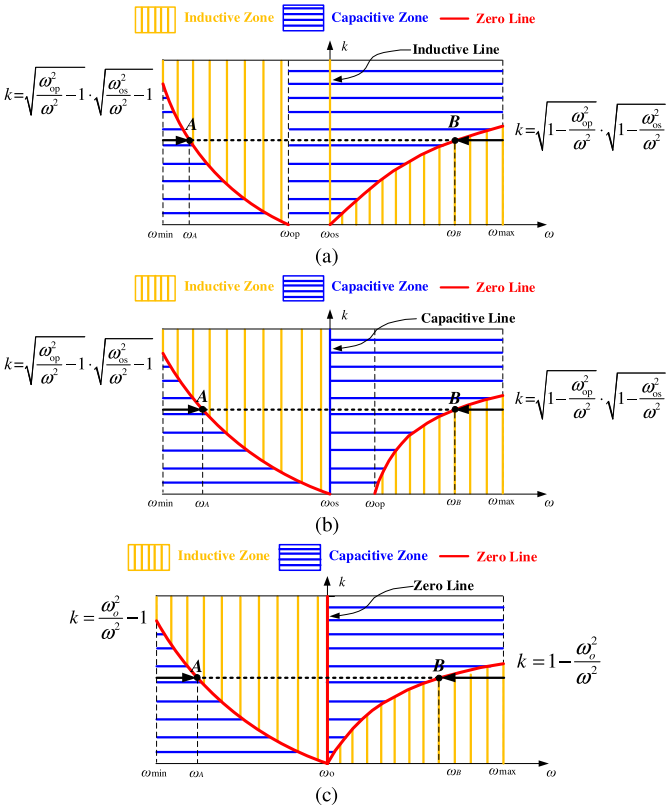

Fig. 3. Characteristics of the equivalent impedance Z_{eq1} in the k–ω plane. (a) $\omega_{op} < \omega_{os}$. (b) $\omega_{op} > \omega_{os}$. (c) $\omega_{op} = \omega_{os} = \omega_o$

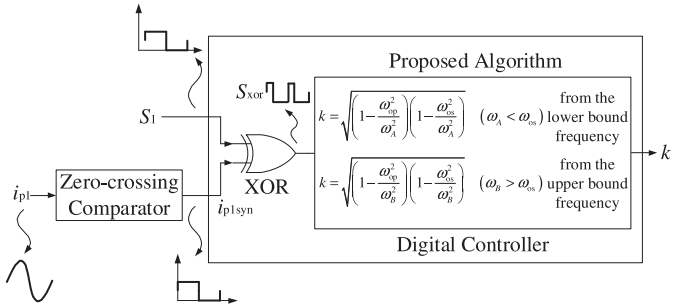

Fig. 4. Block diagram of a digital controller for determination of coupling coefficient.

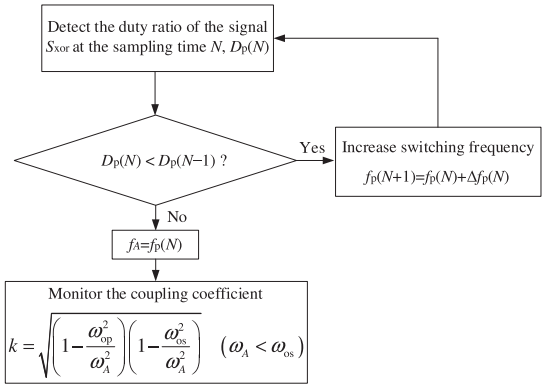

Fig. 5. Flowchart of the monitoring strategy to determine ω_A and then k.

the zero lines across the Point-*A* and the Point-*B* are as follows:

$$k = \sqrt{\frac{\omega_{\rm op}^2}{\omega^2} - 1} \cdot \sqrt{\frac{\omega_{\rm os}^2}{\omega^2} - 1} \tag{6.1}$$

$$k = \sqrt{1 - \frac{\omega_{\rm op}^2}{\omega^2}} \cdot \sqrt{1 - \frac{\omega_{\rm os}^2}{\omega^2}}. \tag{6.2}$$

The corresponding angular frequencies of the Point-*A* and the Point-*B* are ω_A and ω_B, respectively. Based on (6.1) and (6.2), the coupling coefficient of the system can be estimated using

$$k = \sqrt{\frac{\omega_{\rm op}^2}{\omega_A^2} - 1} \cdot \sqrt{\frac{\omega_{\rm os}^2}{\omega_A^2} - 1} \quad (\omega_A < \omega_{\rm os}) \tag{7.1}$$

or

$$k = \sqrt{1 - \frac{\omega_{\rm op}^2}{\omega_B^2}} \cdot \sqrt{1 - \frac{\omega_{\rm os}^2}{\omega_B^2}} \quad (\omega_B > \omega_{\rm os})\,. \tag{7.2}$$

Generally, $C_{\rm p}$ and $C_{\rm s}$ are designed to compensate $L_{\rm p}$ and $L_{\rm s}$ to match the required resonant frequency ω_o in order to minimize the apparent power rating of the power supply and maximize the transfer capability, respectively. If $\omega_{\rm op} = \omega_{\rm os} = \omega_o$, the coupling coefficient k can be monitored using simplified equations

$$k = \frac{\omega_o^2}{\omega_A^2} - 1 \quad (\omega_A < \omega_o) \tag{8.1}$$

or

$$k = 1 - \frac{\omega_o^2}{\omega_B^2} \quad (\omega_B > \omega_o)\,. \tag{8.2}$$

Obviously, the coupling coefficient of the WPT system can be monitored by the determination of the operating frequency at Point-*A* or Point-*B*.

For practical implementation, $i_{\rm p1}$ is sensed and fed to a zero-crossing comparator, as shown in Fig. 4. The output of this comparator ($i_{\rm psyn}$) and the gating signal of the switch Φ_1 (S_1) of the power inverter in the transmitter circuit are fed into an Exclusive-OR (XOR) logic gate, the output of which is labeled as $S_{\rm XOR}$. The gating signal S_1 represents the power inverter's output voltage. When $i_{\rm p1}$ is positive, $i_{\rm psyn}$ is a positive pulse. If the waveforms S_1 and $i_{\rm psyn}$ are in phase, it means that the inverter voltage and the input primary current are in phase. The $S_{\rm XOR}$ signal represents the phase shift between S_1 and $i_{\rm psyn}$. As the pulsewidth of the $S_{\rm XOR}$ signal decreases, the phase shift between S_1 and $i_{\rm psyn}$ decreases. When the pulsewidth of $S_{\rm XOR}$ is zero, the operating Point-*A* (ω_A) or Point-*B* (ω_B) is reached.

In order to determine ω_A, the power inverter's frequency is scanned from the lower bound frequency $f_{\rm min}$. Fig. 5 shows the flowchart of determining ω_A and then k. The duty cycle of the signal $S_{\rm XOR}$ is detected and represented as a digitized signal $D_{\rm p}(N)$. If this duty cycle is smaller than the previous duty cycle (i.e., $D_{\rm p}(N) < D_{\rm p}(N–1)$), the switching frequency will increase. This process will continue until $D_{\rm p}(N)$ approaches zero when

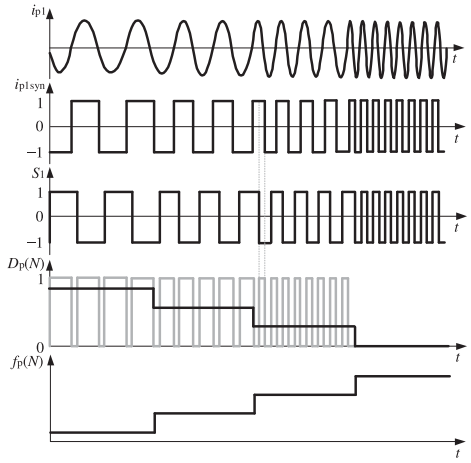

Fig. 6. Timing diagrams of the monitoring strategy to determine ω_A and then k.

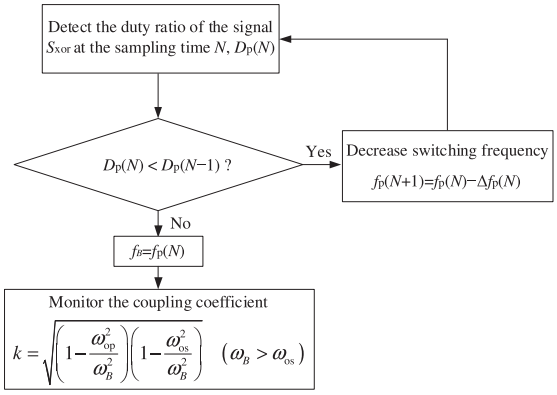

Fig. 7. Flowchart of the monitoring strategy to determine ω_B and then k.

ω_A is reached. Then, the coupling coefficient can be determined from (7.1). The timing diagram of typical waveforms of related signals (in Figs. 4 and 5) is shown in Fig. 6.

In the proposed monitoring strategy for determining ω_B at Point-B from the upper bound frequency $f_{\max}$, $D_p(N)$ is regularly monitored as shown in the flowchart in Fig. 7. If this duty cycle is smaller than the previous duty cycle (i.e., $D_p(N) < D_p(N–1)$), the switching frequency will decrease. This process will continue until $D_p(N)$ approaches zero when ω_B is reached. Then, the coupling coefficient can be determined from (7.2). The timing diagram of typical waveforms of related signals (in Figs. 4 and 7) is shown in Fig. 8.

III. Simulation Results

Simulations are carried out in PSIM 10.0 with the specifications of the SS-compensated WPT system given in Table III. The switching signals S_1, S_3 and S_2, S_4 of the transmitter are complimentary with the duty ratio of 0.5. Both the switches Φ_5 and Φ_6 are consistently closed. The implementation of the proposed monitoring strategy in simulation is depicted in Fig. 9. Initially, the primary current $i_p(N)$ at the sampling time

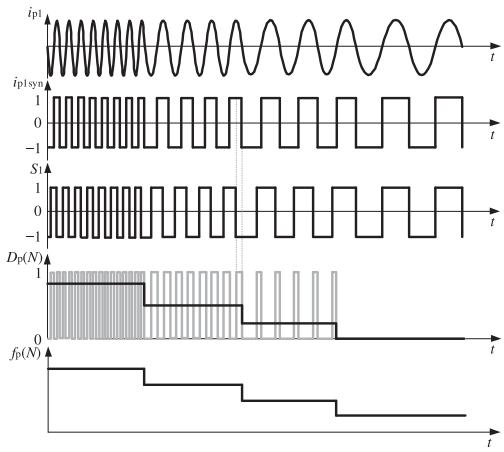

Fig. 8. Timing diagrams of the monitoring strategy to determine ω_B and then k.

TABLE III
Specifications of the WPT System in Simulation

Parameter	Value	Parameter	Value	Parameter	Value
V_{dc}	5 V	C_1~C_6	315 pF	L_p	91.78 μH
C_p	27.6 nF	R_p	0.7 Ω	L_s	92.05 μH
C_s	27.6 nF	R_s	1.01 Ω	C_f	100 μF

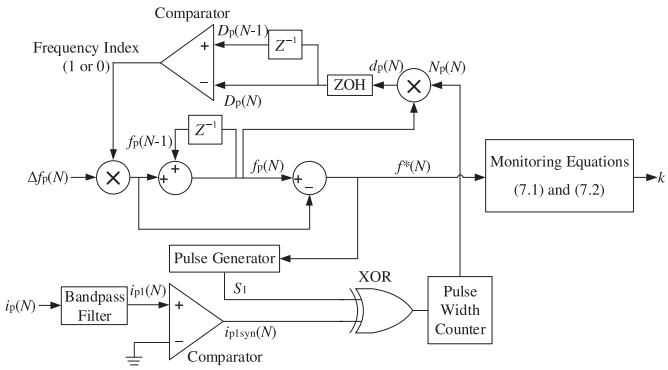

Fig. 9. Hardware implementation of the proposed monitoring strategy.

N is measured. $i_{p1}(N)$ is the fundamental component of $i_p(N)$, which can be obtained by applying a bandpass filter on $i_p(N)$. $i_{p1syn}(N)$ is the synchronous pulse signal of $i_{p1}(N)$. The XOR of $i_{p1syn}(N)$ and S_1 results in the difference pulse signal that indicates the phase difference between $i_{p1}(N)$ and $v_{p1}(N)$. $N_p(N)$ is the counted pulsewidth of the difference pulse signal. The duty ratio of the difference pulse signal, i.e., $d_p(N)$, is calculated by multiplying $N_p(N)$ and the switching frequency $f_p(N)$. By using a zero-order holder and the delay sampling (Z^{-1}) by one cycle, discrete duty ratios of the difference pulse signal at the sampling time N–1 and N, i.e., $D_p(N–1)$ and $D_p(N)$, can be obtained (the discrete duty ratios can prevent the erroneous results of the frequency index caused by the dynamics of d_p during the frequency sweep). Compare $D_p(N–1)$ with $D_p(N)$, if $D_p(N–1) > D_p(N)$, the frequency index is 1, which means the switching frequency $f_p(N–1)$ of the transmitter inverter at the sampling time N–1 can be further increased (search from $f_{\min}$) or decreased

TABLE IV
PARAMETERS OF THE MONITORING STRATEGY IN SIMULATION

Case Number		f_{min}/f_{max}	Δf_p	f_{step}	f_A/f_B	$R_{err}(\%)$	T_{mon}
1	from f_{min}	90 kHz	0.2 kHz	0.5 kHz	92.4 kHz	0.75	30 ms
	from f_{max}	110 kHz	–0.2 kHz	0.5 kHz	109.6 kHz	1.46	10 ms
2.1		145 kHz	–0.2 kHz	0.5 kHz	140 kHz	0.04	56 ms
2.2		145 kHz	–0.2 kHz	0.5 kHz	141.2 kHz	0.08	44 ms
2.3		145 kHz	–0.2 kHz	0.5 kHz	142.8 kHz	0.32	28 ms

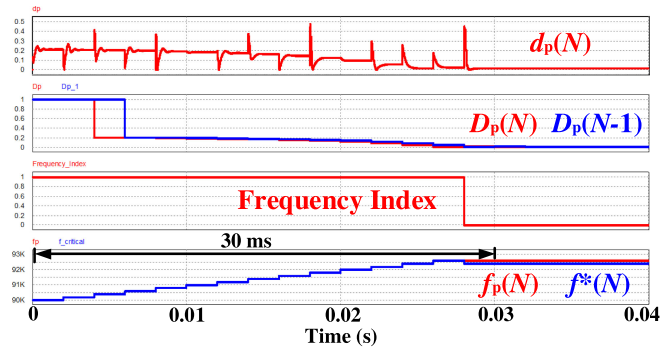

Fig. 10. Waveforms of the variables of the monitoring strategy for determining ω_A through frequency sweep from the lower bound in case 1.

(search from f_{max}) by a frequency step $|\Delta f_p(N)|$, i.e., $\Delta f_p(N) > 0$ for the search from f_{min} and $\Delta f_p(N) < 0$ for the search from f_{max}. If $D_p(N\text{–}1) \leq D_p(N)$, the frequency index is 0, which means the switching frequency $f_p(N\text{–}1)$ of the transmitter inverter at the sampling time N–1 cannot be further increased or decreased. $f_p(N\text{–}1)$ can be considered as the critical frequency $f^*(N)$, i.e., $f^*(N) = f_p(N\text{–}1) = f_p(N)\text{–}\Delta f_p(N)$. The critical frequency is the operating frequency at the Point-*A* or Point-*B*. Then the coupling coefficient k can be monitored based on (7.1) or (7.2).

In simulation, two cases of the coupling coefficient monitoring for SS-compensated WPT systems are presented. The main parameters of the monitoring strategy are provided in Table IV. Here, f_{step} is the frequency of the step change Δf_p. R_{err} is the relative error between the actual and monitored coupling coefficient. T_{mon} is the total monitoring time (the computation time is negligible as compared to the searching time).

A. Case 1: Coupling Coefficient of the WPT System is 0.17

In case 1, the coupling coefficient of the WPT system is 0.17. The specifications of the WPT system are identical to those in Table III. The resonant frequencies of both the transmitter and the receiver circuit are 100 kHz. Fig. 10 contains typical waveforms of $d_p(N)$, $D_p(N)$, $D_p(N\text{–}1)$, Frequency Index, $f_p(N)$ and $f^*(N)$ in the monitoring strategy of Fig. 9. At the initial stage of the search process, the phase shift between v_p and i_p is relatively large as reflected from the magnitude of $d_p(N)$ and $D_p(N)$. As the switching frequency of the inverter increases, this phase shift decreases until $D_p(N)$ approaches zero. Then, the critical frequency f_A (and thus ω_A) is determined. Once ω_A is found, the coupling coefficient k can be monitored based on (8.1).

Fig. 11 shows the typical waveforms of v_p and i_p in the transmitter circuit. Here, θ is the phase difference between i_{p1} and v_{p1}. It can be seen that, before ω_A is determined, the input current and input voltage of the primary coil-resonator are not in phase (i.e., $\cos\theta = 0.217$). Fig. 12 shows the corresponding waveforms after ω_A is determined. It is noted that i_{p1} and v_{p1} are now essentially in phase (i.e., $\cos\theta = 0.99$). Based on (8.1), the monitored coupling coefficient is 0.1713, which is close to the target value of 0.17. The relative error and total monitoring time are given in Table IV.

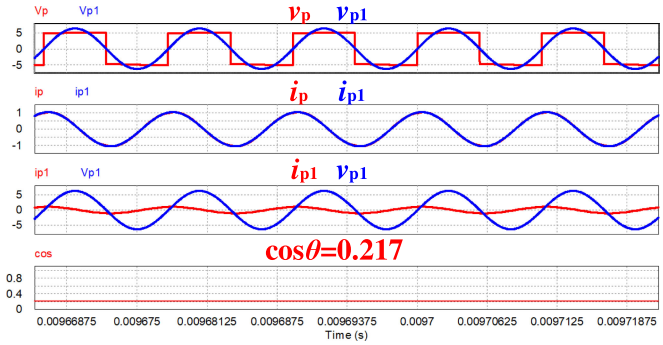

Fig. 11. Waveforms of voltage and current and their phase in the transmitter circuit at the lower bound of $f_{min} = 90$ kHz before f_A is reached in case 1.

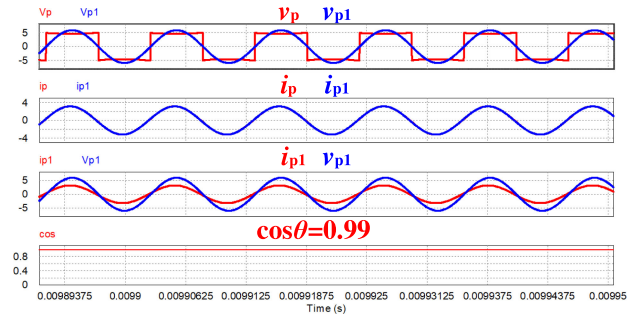

Fig. 12. Waveforms of voltage and current and their phase in the transmitter circuit after f_A of 92.4 kHz is reached in case 1.

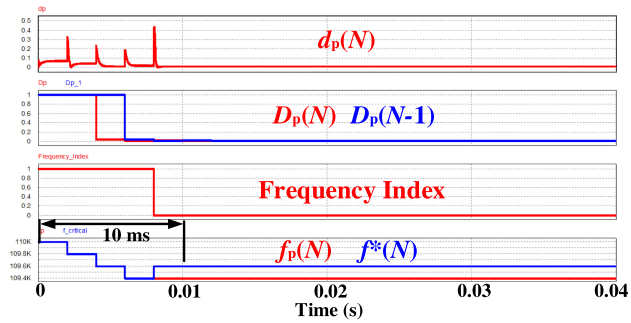

Fig. 13. Waveforms of the variables of the monitoring strategy for determining ω_B through frequency sweep from the upper bound in case 1.

Starting from the upper bound frequency of 110 kHz, this test demonstrates the determination of ω_B. The results are shown in Figs. 13–15. As expected, the frequency f_B can be located quickly, as shown in Fig. 13. Before f_B is located, there is obvious phase shift between v_p and i_p (i.e., $\cos\theta = 0.898$), as shown in Fig. 14. When f_B is located, v_p and i_p are in phase

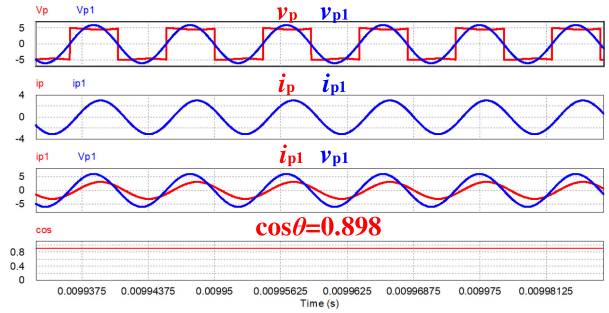

Fig. 14. Waveforms of voltage and current and their phase in the transmitter circuit at the upper bound of $f_{\max} = 110$ kHz before f_B is reached in case 1.

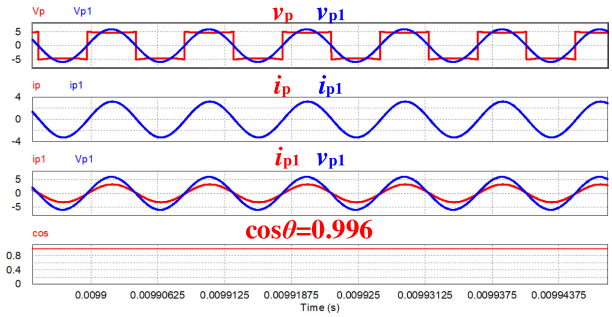

Fig. 15. Waveforms of voltage and current and their phase in the transmitter circuit after f_B of 109.6 kHz is reached in case 1.

(i.e., $\cos\theta = 0.996$), as shown in Fig. 15. Based on (8.2), the monitored coupling coefficient is 0.1675, which is close to the target value of 0.17. The relative error and total monitoring time are provided in Table IV.

B. Case 2: Coupling Coefficient of the WPT System is 0.5 and the Resonant Frequencies of the Transmitter are 98, 100 and 102 kHz

In case 2, the coupling coefficient of the WPT system is 0.5. The compensated capacitors of the transmitter are 28.7, 27.6, and 26.5 nF for cases 2.1, 2.2, and 2.3, respectively. The other parameters of the WPT system are the same as the parameters given in Table III. The resonant frequency of the receiver is 100 kHz. The resonant frequencies of the transmitter are 98, 100, and 102 kHz for cases 2.1, 2.2, and 2.3, respectively. Fig. 16 shows the waveforms of $d_{\rm p}(N)$, $D_{\rm p}(N)$, $D_{\rm p}(N–1)$, Frequency Index, $f_{\rm p}(N)$ and $f^*(N)$ in case 2. At the initial stages of the search processes, the phase shifts between $v_{\rm p}$ and $i_{\rm p}$ are relatively large as reflected from the magnitudes of $d_{\rm p}(N)$ and $D_{\rm p}(N)$. As the switching frequency of the inverter decreases, the phase shift decreases until $D_{\rm p}(N)$ approaches zero for all the three cases. Then, ω_B are determined and the coupling coefficient k can be further monitored based on (7.2) as 0.4998, 0.4984, and 0.4996. The relative errors and total monitoring time are given in Table IV. All relative errors in the cases 1 and 2 are less than 1.5%. Besides, for the SS-compensated WPT system with a stronger coupling, the proposed monitoring strategy is more accurate (relative errors in case 2 are much less than those in case 1).

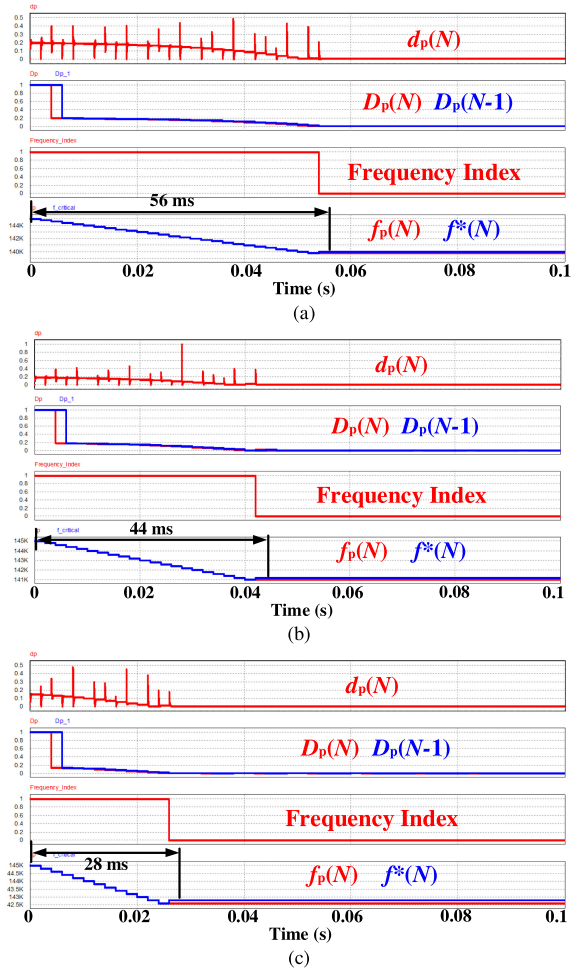

Fig. 16. Waveforms of the variables of the monitoring strategy for determining ω_B through frequency sweep from the upper bound in case 2. (a) $\omega_{\rm op} = 98$ kHz. (b) $\omega_{\rm op} = 100$ kHz. (c) $\omega_{\rm op} = 102$ kHz.

IV. Experimental Verification

Experiments are carried out on the SS-compensated WPT systems with S-BAR rectifiers and three types of resonators. The photographs of these resonators are shown in Fig. 17. The coils of the resonators-I are helical, while the coils of the resonators-II and the resonators-III are planar. For the resonators-I and the resonators-II, the diameters of the transmitter coil and the receiver coil are the same. For the resonators-III, the coil diameters are different. The specifications of the three resonators are tabulated in Tables V–VII, respectively. The full schematic diagram of the WPT system in the experiment is depicted in Fig. 18. No wireless communication system is used between the transmitter and the receiver. For the transmitter, a hall-effect current sensor LA12-10V21 is used to measure the transmitter circuit. The output of the current sensor can be directly feedback to the analog-to-digital-conversion pin of the transmitter controller, i.e., Texas Instruments F28379D Delfino Experimenter Kit.

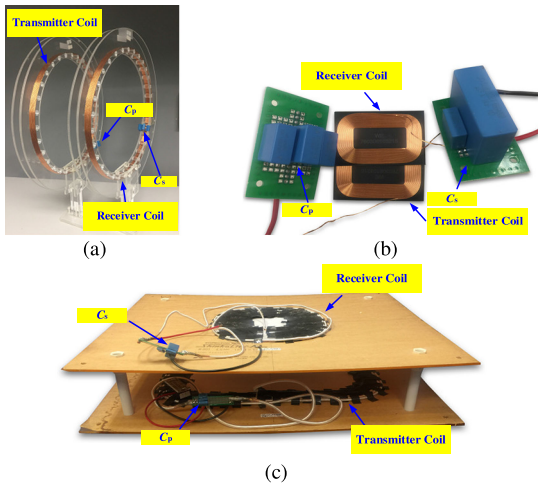

Fig. 17. Photographs of the three types of resonators in experiment. (a) Resonators-I. (b) Resonators-II. (c) Resonators-III.

TABLE V
SPECIFICATIONS OF THE RESONATORS-I

Parameter	Value
Coil diameter of both transmitter and receiver coils	31 cm
Wire diameter of both transmitter and receiver coils	1.2 mm
Number of turns of transmitter and receiver coils	11
Length of the winding of transmitter and receiver coils	15 mm
L_p @ 100 kHz	91.78 μH
C_p @ 100 kHz	27.2 nF
R_p @ 100 kHz	0.95 Ω
L_s @ 100 kHz	92.05 μH
C_s @ 100 kHz	26.9 nF
R_s @ 100 kHz	1.06 Ω

TABLE VI
SPECIFICATIONS OF THE RESONATORS-II

Parameter	Value
Number of strings for both transmitter and receiver	1
Wire diameter of both transmitter and receiver coils	1 mm
Length of the winding of transmitter and receiver coils	48 mm
L_p @ 100 kHz	14.3 μH
C_p @ 100 kHz	177.4 nF
R_p @ 100 kHz	0.1 Ω
L_s @ 100 kHz	14.3 μH
C_s @ 100 kHz	177.3 nF
R_s @ 100 kHz	0.1 Ω

TABLE VII
SPECIFICATIONS OF THE RESONATORS-III

Parameter	Value
Number of strings for the transmitter coil	7
Wire outer diameter of the transmitter coil	6.5 mm
Number of strings for the receiver coil	15
Wire outer diameter of the receiver coil	4.3 mm
Number of turns of transmitter and receiver coils	11
L_p @ 85 kHz	46.12 μH
C_p @ 85 kHz	76.1 nF
R_p @ 85 kHz	0.37 Ω
L_s @ 85 kHz	60.46 μH
C_s @ 85 kHz	58 nF
R_s @ 85 kHz	0.09 Ω

The phase delay of the hall-effect sensor and a phase difference between S_1 and v_{p1} at the critical frequencies can be tuned offline and compensated in the controller to ensure the equivalent impedance Z_{eq} is pure-resistive (i.e., v_{p1} and i_{p1} are in phase) at critical frequencies (i.e., ω_A and ω_B). The proposed monitoring strategy is implemented in the transmitter controller. In this article, due to the high-order harmonics of the transmitter current i_p are negligible for all the investigated systems, the measured waveforms of i_p and its fundamental component i_{p1} are almost identical. The switching frequency f_p of the monitoring strategy is exported via the digital-to-analog-conversion (DAC) pin of the transmitter controller. The linear relationship between the output voltages of the DAC pin (i.e., v_{fp}) and the actual switching frequency (i.e., f_p) are proportionally tuned. The main parameters of the monitoring strategy are provided in Table VIII. For the receiver, both switches of the S-BAR rectifier are controlled to be turned ON by the receiver controller, i.e., TMS320F28335 Experimenter Kit. The parameters v_p, i_p, and v_{fp} are measured by the Keysight DSOS054A High-Definition Oscilloscope. As the phase differences between i_p and the fundamental component i_{p1} are negligible for all the resonator types, the phase difference between v_{p1} and i_p can be considered as the phase difference between v_{p1} and i_{p1}.

A. *Resonators-I With Different Distances Between the Coils*

For the SS-compensated WPT system with the resonators-I, the dc source voltage (i.e., V_{dc}) is 5 V. The distance between the coils is initially 10 cm. The corresponding coupling coefficient is preliminarily measured to be 0.17. The waveforms of v_p, v_{p1}, i_p, and v_{fp} of the WPT system operating at the lower bound are shown in Fig. 19(a). i_p leads v_{p1} about 86.72°. The equivalent reactance of the system (i.e., X_{eq1}) is capacitive, which validates the analysis of the characteristics in Table II and Fig. 3. The output voltage of the DAC pin (i.e., v_{fp}) is at the minimum (i.e., v_{fmin}) of 1.61 V, which indicates the operating frequency of the WPT system is at the minimum (i.e., f_{min}) of 90 kHz. Then, the operating frequency sweeps from f_{min} to the critical frequency f_A. The transmitter controller finds the critical frequency at 93.2 kHz and maintains the operating frequency at f_A. The waveforms of v_p, v_{p1}, i_p, and v_{fp} during the search are shown in Fig. 19(b). v_{fp} is searched from 1.61 V (v_{fmin}) to 2.97 V with the voltage step of 0.08 V and then reduced from 2.97 to 2.89 V (v_{fA}) in the next step, which signifies that the operating frequency of the WPT system is changed from 90 to 93.4 kHz with the frequency step of 0.2 kHz and then reduced from 93.4 kHz to the critical frequency 93.2 kHz. The steady-state waveforms of v_p, v_{p1}, i_p, and v_{fp} of the WPT system operating at f_A are shown in Fig. 19(c). v_{p1} and i_p are in phase (the phase difference between v_{p1} and i_p is approximately null). The operating frequency is 93.2 kHz. Based on (7.1), the monitored coupling coefficient from the lower bound can be calculated as 0.1728. The relative errors and total monitoring time are provided in Table VIII.

The switching frequency of the transmitter inverter (i.e., f_p) also sweeps from the upper bound (i.e., f_{max}) of 115 kHz

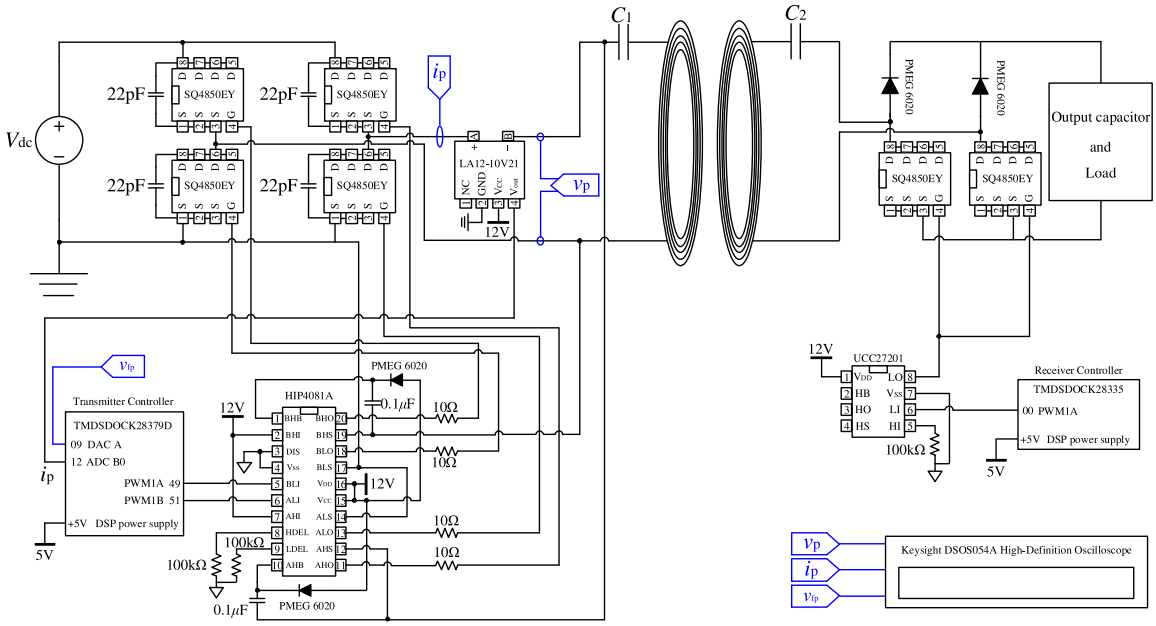

Fig. 18. Full hardware schematic diagram of the WPT system in experiment.

TABLE VIII
PARAMETERS OF THE MONITORING STRATEGY IN EXPERIMENT

Resonator Type		f_{min}/f_{max} (v_{fp})	Δf_p (v_{fp})	f_{step}	f_A/f_B	R_{err}(%)	T_{mon}
1	10 cm, from f_{min}	90 kHz (1.61 V)	0.2 kHz (0.08 V)	0.5 kHz	93.2 kHz (2.89 V)	1.65	38 ms
	10 cm, from f_{max}	115 kHz (2.89 V)	−0.2 kHz (−0.08 V)	0.5 kHz	110.6 kHz (1.13 V)	1.71	50 ms
	18 cm, from f_{max}	110 kHz (2.89 V)	−0.2 kHz (−0.08 V)	0.5 kHz	104.8 kHz (0.81 V)	4.87	58 ms
2	from f_{max}	140 kHz (2.89 V)	−0.2 kHz (−0.08 V)	0.5 kHz	137.6 kHz (1.93 V)	0.53	30 ms
3	from f_{min}	70 kHz (0.81 V)	0.2 kHz (0.08 V)	0.5 kHz	75.6 kHz (3.05 V)	1.27	62 ms

with the step (i.e., Δf_p) of –0.2 kHz. The waveforms of v_p, v_{p1}, i_p, and v_{fp} of the WPT system operating at the upper bound are presented in Fig. 20(a). i_p lags v_{p1} about 75.97°. The equivalent reactance of the system (i.e., X_{eq1}) is inductive, which also verifies the analysis of the characteristics in Table II and Fig. 3. Then, the operating frequency sweeps from f_{max} to the critical frequency f_B. The transmitter controller finds the critical frequency at 110.6 kHz and maintains the operating frequency at f_B. The waveforms of v_p, v_{p1}, i_p, and v_{fp} of the WPT system during the frequency sweep and operating at f_B are exhibited in Fig. 20(b) and (c), respectively. At the steady state, v_{p1} and i_p are in phase. Based on (7.2), the monitored coupling coefficient from the upper bound can be calculated as 0.1671. The relative errors and total monitoring time are provided in Table VIII.

Then, the distance between the coils is changed to 18 cm. The corresponding coupling coefficient is 0.075. The waveforms of v_p, v_{p1}, i_p, and v_{fp} of the WPT system during the frequency sweep and operating at f_B are shown in Fig. 21(a) and (b), respectively. At the steady state, v_{p1} and i_p are in phase. Based on (7.2), the monitored coupling coefficient from the upper bound can be calculated as 0.0723. The relative errors and total monitoring time are provided in Table VIII.

Experiments are also conducted to monitor coupling coefficients of the WPT system with the coil distance of 18 cm from the lower bound and the WPT systems with coil distances of 12, 14, and 16 cm from both the lower and upper bounds (the waveforms are not presented in this article). The overall all results of the WPT systems with the resonators-I are listed in Table IX. Obviously, all the relative errors are less than 5%. The relative errors of the coupling coefficient estimation from either the lower bound or the upper bounds increase when the distance is increased from 10 to 18 cm, indicating that the monitoring method is more accurate when the coupling of the coils is stronger. Besides, the relative error of the monitoring method from the upper bound is larger than that from the lower bound for each distance. The lower and upper bounds of the switching frequency are set to be 90 and 115 kHz for the coils with the distance of 10 cm, while the frequency bounds are set to be 90 and 110 kHz for the coils with the distance of 12 and 14 cm, and 95 and 110 kHz for the coils with the distance of 16 and 18 cm. By using the same frequency bounds, the monitoring time from either the lower bound or the upper bound will be increased when the distance is increased. The monitoring times for all the distances are less than 62 ms.

B. Resonators-II and Resonators-III

For the SS-compensated WPT system with the resonators-II, the dc source voltage (i.e., V_{dc}) is 3.3 V. The actual coupling coefficient is 0.47. The waveforms of v_p, v_{p1}, i_p, and v_{fp} during the search process are presented in Fig. 22. Based on (7.2), the monitored coupling coefficient from the upper bound for the WPT system with the resonators-II can be calculated as 0.4725.

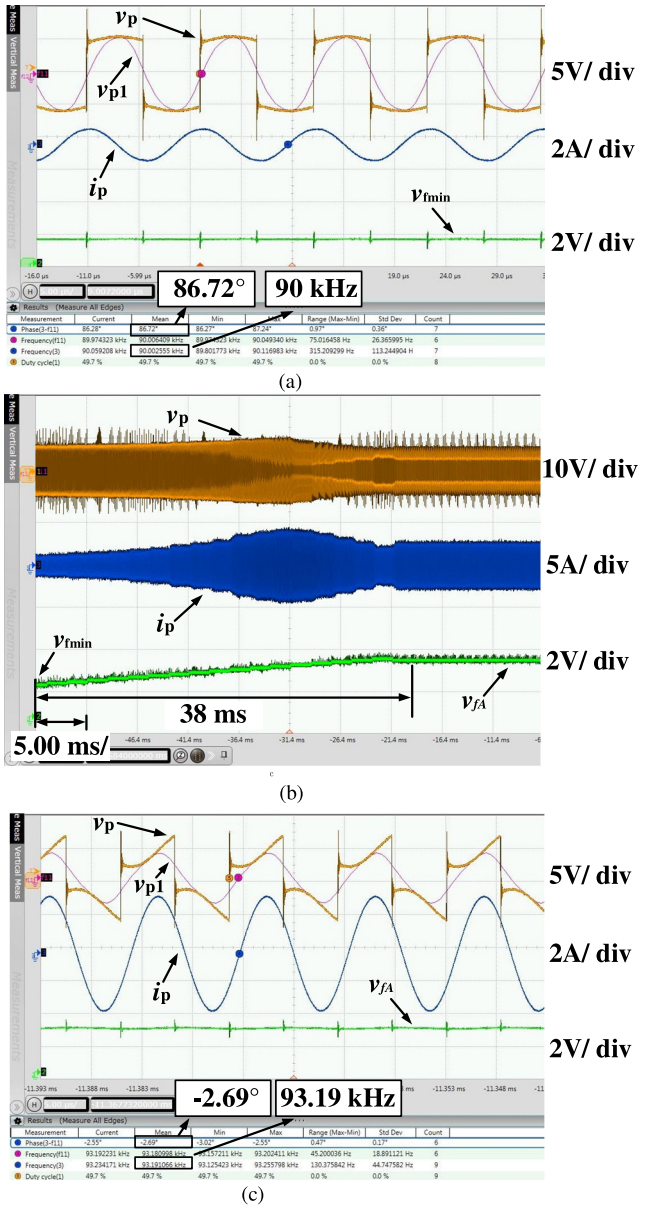

Fig. 19. Waveforms of $v_{\rm p}$, $v_{\rm p1}$, $i_{\rm p}$, and $v_{\rm fp}$ of the WPT system operating from 90 to 93.2 kHz with the resonators-I (10 cm distance between the coils, $k = 0.17$). (a) At 90 kHz ($f_{\rm min}$). (b) From 90 ($f_{\rm min}$) to 93.2 kHz (f_A). (c) At 93.2 kHz (f_A).

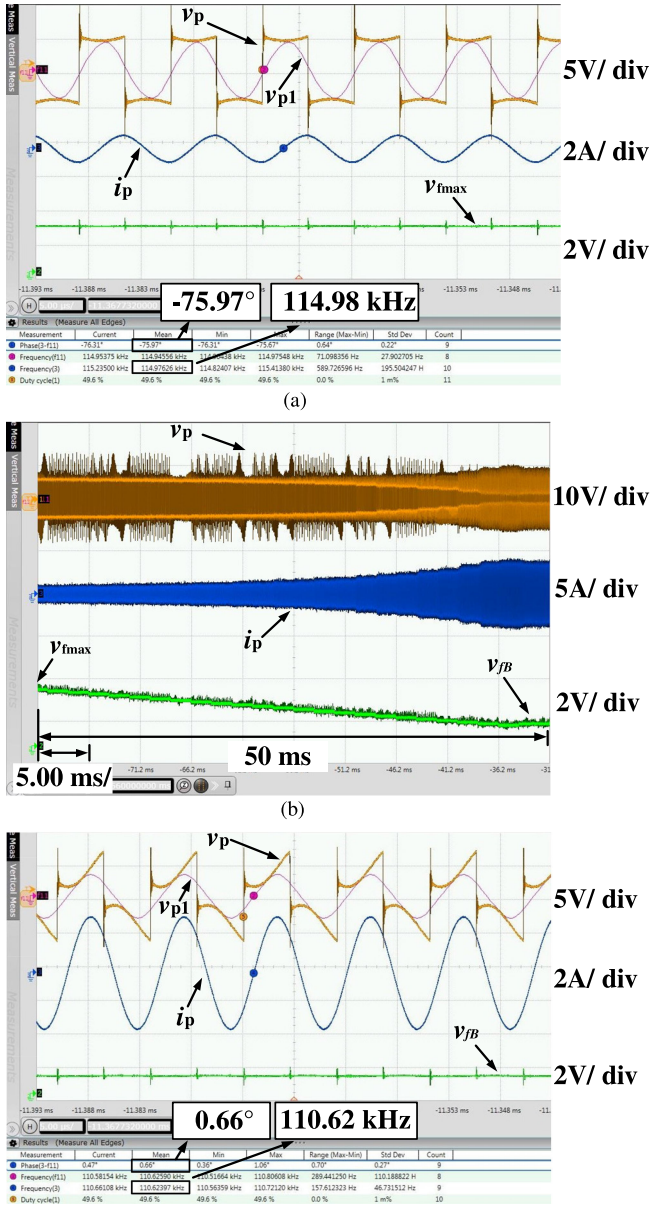

Fig. 20. Waveforms of $v_{\rm p}$, $v_{\rm p1}$, $i_{\rm p}$, and $v_{\rm fp}$ of the WPT system operating from 115 to 110.6 kHz with the resonators-I (10 cm distance between the coils, $k = 0.17$). (a) At 115 kHz ($f_{\rm max}$). (b) From 115 ($f_{\rm max}$) to 110.6 kHz (f_B). (c) At 110.6 kHz (f_B).

The relative errors and total monitoring time are provided in Table VIII. Similarly, the monitored coupling coefficient from the lower bound can be calculated as 0.4639. The relative error is 1.3% and the monitoring time is 42 ms.

For the SS-compensated WPT system with the resonators-III, the dc source voltage (i.e., $V_{\rm dc}$) is 12 V. The actual coupling coefficient is 0.26. The waveforms of $v_{\rm p}$, $v_{\rm p1}$, $i_{\rm p}$, and $v_{\rm fp}$ during the frequency sweep are shown in Fig. 23. Based on (7.1), the monitored coupling coefficient from the lower bound for the WPT system with the resonators-III can be calculated as 0.2633. The relative errors and total monitoring time are provided in Table VIII. Similarly, the monitored coupling coefficient from the upper bound can be calculated as 0.2573. The relative error is 1.04% and the monitoring time is 46 ms.

C. Comparisons Among the Proposed Monitoring Strategy and the Existing Monitoring Strategies

The coupling coefficients of the WPT systems with the resonators-I, II, and III are also monitored by the existing monitoring strategies in [18], [20], and [21], respectively. For the monitoring strategy in [20], the equivalent load resistance is primarily estimated. Then, the coupling coefficient is further monitored at the resonant frequency using

$$k = \sqrt{\frac{\left(\frac{V_{\rm p1}}{I_{\rm p1}} - R_{\rm p}\right)\left(R_s + \tilde{R}_L\right)}{\omega_o^2 L_{\rm p} L_s}} \quad (\omega = \omega_o) \tag{9}$$

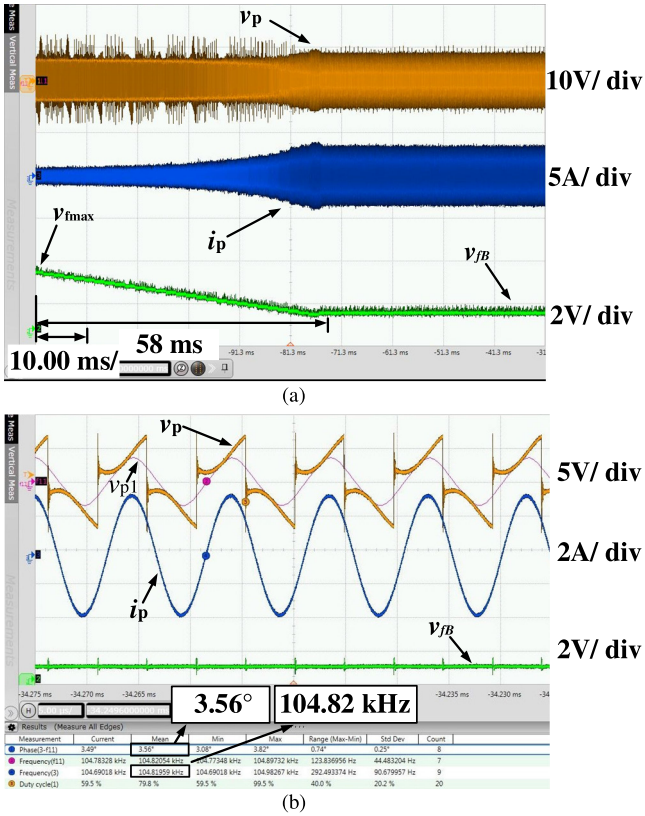

Fig. 21. Waveforms of $v_{\rm p}$, $v_{\rm p1}$, $i_{\rm p}$, and $v_{\rm fp}$ of the WPT system operating from 110 to 104.8 kHz with the resonators-I (18 cm distance between the coils, $k = 0.075$). (a) From 110 ($f_{\max}$) to 104.8 kHz (f_B). (b) At 104.8 kHz (f_B).

TABLE IX
COMPREHENSIVE RESULTS OF THE RESONATORS-I

Distance	Actual k	Monitored k		$R_{\rm err}$(%)	$T_{\rm mon}$ (ms)
10 cm	0.17	from lower bound	0.1728	1.65	38
		from upper bound	0.1671	1.71	50
12 cm	0.136	from lower bound	0.1384	1.76	52
		from upper bound	0.1329	2.28	22
14 cm	0.111	from lower bound	0.1194	2.05	60
		from upper bound	0.1134	3.08	34
16 cm	0.092	from lower bound	0.0962	2.34	20
		from upper bound	0.09	4.26	48
18 cm	0.076	from lower bound	0.0782	2.89	28
		from upper bound	0.0723	4.87	58

where $V_{\rm p1}$ and $I_{\rm p1}$ are the amplitudes of $v_{\rm p1}$ and $i_{\rm p1}$. $\tilde{R}_L$ is the estimated equivalent load resistance. The comparisons among the proposed monitoring strategy and the existing monitoring strategies are conducted on the WPT systems with the deviations of ESR of the resonators, which always occurs when the temperature and operating frequency alter. In experiment, the practical deviations of ESR are emulated by the deviations of the parameter values of ESR being adopted for the monitoring strategies in the transmitter controller.

First, the proposed monitoring strategy and the monitoring strategies in [18], [20], and [21] are adopted to monitor the coupling coefficient of the WPT system with the resonators-I and the distance between the coils is 10 cm. Fig. 24 shows the

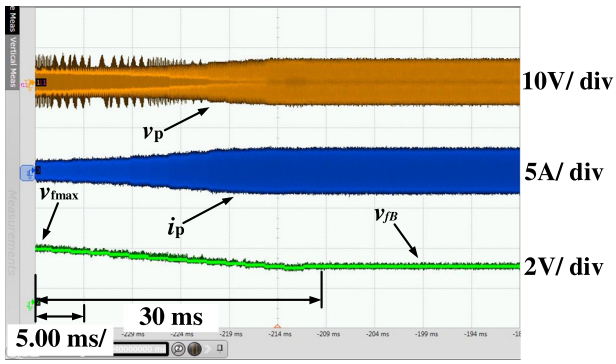

Fig. 22. Waveforms of $v_{\rm p}$, $v_{\rm p1}$, $i_{\rm p}$ and $v_{\rm fp}$ of the WPT system operating from 140 to 137.6 kHz with the resonators-II ($k = 0.47$).

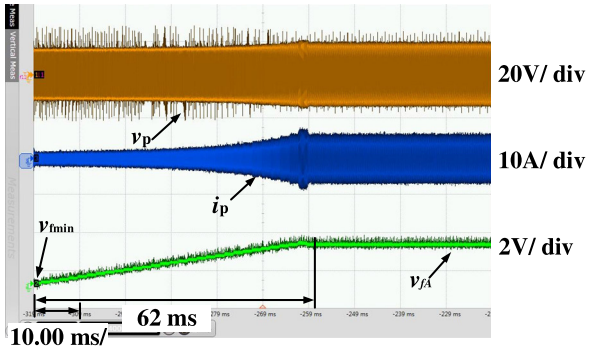

Fig. 23. Waveforms of $v_{\rm p}$, $v_{\rm p1}$, $i_{\rm p}$, and $v_{\rm fp}$ of the WPT system operating from 70 to 75.6 kHz with the resonators-III ($k = 0.26$).

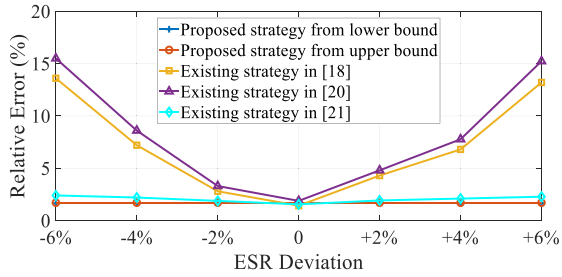

Fig. 24. Comparative curves of the monitoring errors for the WPT system with the resonators-I.

TABLE X
AVERAGE MONITORING TIME FOR RESONATORS-I

Distance	Proposed strategy	Strategy in [21]
10 cm	44 ms	15 s
12 cm	37 ms	14.7 s
14 cm	47 ms	14.9 s
16 cm	34 ms	15.1 s
18 cm	43 ms	14.9 s

comparative curves of the relative errors among the proposed monitoring strategy and the existing monitoring strategies when the ESR of the transmitter coil deviates about $\pm 2\%$, $\pm 4\%$, and $\pm 6\%$, while the ESR of the receiver coil remains unchanged. It can be seen that the relative errors of the proposed monitoring strategy are much less than those of the monitoring strategy

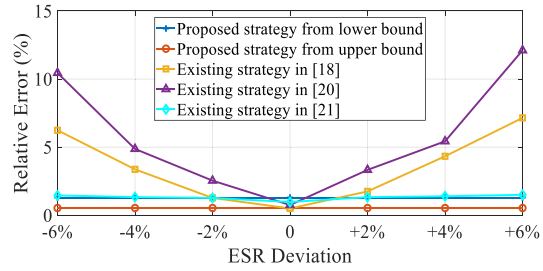

Fig. 25. Comparative curves of the monitoring errors for the WPT system with the resonators-II.

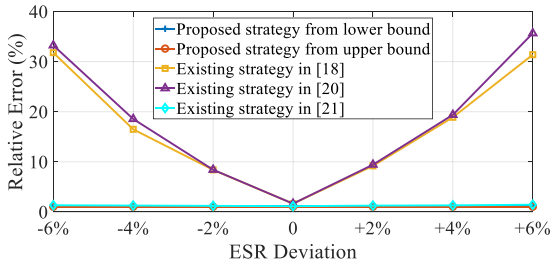

Fig. 26. Comparative curves of the monitoring errors for the WPT system with the resonators-III.

in [18] and [20] when the ESR of the transmitter coil deviates from the nominal value. The discrepancy of the relative errors becomes larger as the deviation increases. Besides, the relative errors of both the proposed monitoring strategy and the monitoring strategy in [21] are steady and small. However, the average monitoring time of the proposed strategy is much less than that of the strategy in [21]. A comparison of the average monitoring time between the proposed strategy and the strategy in [21] for the coil distances of 10, 12, 14, 16, and 18 cm is given in Table X. The average monitoring time of the proposed strategy are only tens of milliseconds, which is much shorter than the average monitoring time of the strategy in [21] (the processor used is Intel(R)Core(TM) i5-2400 CPU@3.10 GHz).

Similarly, comparisons are also conducted on the WPT systems with the resonators-II and the resonators-III. Figs. 25 and 26 show the comparative curves of the monitoring errors when the ESR of both resonators deviate about $\pm 2\%$, $\pm 4\%$, and $\pm 6\%$ for the WPT system with the resonator-II and resonator-III, respectively. The proposed monitoring strategy exhibits much higher accuracy than the existing monitoring strategies in [18] and [20] when the ESR of the resonators deviates from its nominal value. Besides, the average identification time of the proposed monitoring strategy and the monitoring strategy in [21] is about 37 ms and 15 s for the WPT system with the resonator-II, and 57 ms and 20 s for the WPT system with the resonator-III, respectively. The proposed monitoring strategy is demonstrated to identify the coupling coefficients much faster than the existing monitoring strategy in [21].

V. Conclusion

This article presents a fast hardware approach to front-end monitoring strategy for mutual coupling coefficient in SS-compensated WPT systems with active rectifiers. The novel method is not a traditional model-based method. It has the advantage that it requires only the knowledge of the operating frequency range specified in the wireless charging standard and does not need the knowledge of the transmitter and receiver coil resonator parameters. Without using any extra wireless communication system between the transmitter and the receiver, the proposed method can monitor the mutual coupling coefficient based on the frequency sweep from either the lower bound or upper bound after shorting the rectifier output to the secondary ground. The proposed method can determine the mutual coupling coefficient within 62 ms typically while other existing model-based methods take seconds or minutes to do the estimation. The hardware can be implemented in inexpensive digital controllers. Both simulation and experimental results validate the accuracy of the proposed monitoring strategy for both strongly and weakly coupled resonators. Experimental results also exhibit that the proposed monitoring strategy is generally applicable for WPT systems with helical/planar coils, and same/different diameters of the transmitter and receiver coils. Comparative studies of the three different WPT systems have demonstrated that the proposal is more robust (less sensitive to ESR), faster in determining the mutual coupling coefficient and requires less sensor than existing monitoring strategies.

References

[1] C. T. Rim and C. Mi, *Wireless Power Transfer for Electric Vehicles and Mobile Devices*. Chichester, U.K.: Wiley, 2017.

[2] W. X. Zhong and S. Y. R. Hui, "Maximum energy efficiency tracking for wireless power transfer systems," *IEEE Trans. Power Electron.*, vol. 30, no. 7, pp. 4025–4034, Jul. 2015.

[3] D. Patil, M. Sirico, L. Gu, and B. Fahimi, "Maximum efficiency tracking in wireless power transfer for battery charger: Phase shift and frequency control," in *Proc. IEEE Energy Convers. Congr. Expo.* 2016, pp. 1–8.

[4] T. D. Yeo, D. Kwon, S. T. Khang, and J. W. Yu, "Design of maximum efficiency tracking control scheme for closed-loop wireless power charging system employing series resonant tank," *IEEE Trans. Power Electron.*, vol. 32, no. 1, pp. 471–478, Jan. 2017.

[5] Z. Li, C. Zhu, J. Jiang, K. Song, and G. Wei, "A 3-kW wireless power transfer system for sightseeing car supercapacitor charge," *IEEE Trans. Power Electron.*, vol. 32, no. 5, pp. 3301–3316, May 2017.

[6] Y. Yang, W. Zhong, S. Kiratipongvoot, S. C. Tan, and S. Y. R. Hui, "Dynamic improvement of series-series compensated wireless power transfer systems using discrete sliding mode control," *IEEE Trans. Power Electron.*, vol. 33, no. 7, pp. 6351–6360, Jul. 2018.

[7] Z. Huang, S. C. Wong, and C. K. Tse, "Control design for optimizing efficiency in inductive power transfer systems," *IEEE Trans. Power Electron.*, vol. 33, no. 5, pp. 4523–4534, May 2018.

[8] S. Y. Hui, "Planar wireless charging technology for portable electronic products and Qi," *Proc. IEEE*, vol. 101, no. 6, pp. 1290–1301, Jun. 2013.

[9] T. Diekhans and R. W. De Doncker, "A dual-side controlled inductive power transfer system optimized for large coupling factor variations and partial load," *IEEE Trans. Power Electron.*, vol. 30, no. 11, pp. 6320–6328, Nov. 2015.

[10] G. Lovison, M. Sato, T. Imura, and Y. Hori, "Secondary-side-only simultaneous power and efficiency control for two converters in wireless power transfer system," in *Proc. 41st Annu. Conf. IEEE Ind. Electron. Soc.*, 2015, pp. 4824–4829.

[11] W. Zhong and S. Y. R. Hui, "Charing time control of wireless power transfer systems without using mutual coupling information and wireless communication system," *IEEE Trans. Ind. Electron.*, vol. 64, no. 1, pp. 228–235, Jan. 2017.

[12] Z. Li, K. Song, J. Jiang, and C. Zhu, "Constant current charging and maximum efficiency tracking control scheme for supercapacitor wireless charging," *IEEE Trans. Power Electron.*, vol. 33, no. 10, pp. 9088–9100, Oct. 2018.

[13] Y. Yang, S. C. Tan, S. Y. R. Hui, "Communication-free control scheme for Qi-compliant wireless power transfer systems," in *Proc. IEEE Energy Convers. Congr. Expo.*, 2019, pp. 4955–4960.
[14] Y. Li, J. Hu, F. Chen, Z. Li, Z. He, and R. Mai, "Dual-phase-shift control scheme with current-stress and efficiency optimization for wireless power transfer systems," *IEEE Trans. Circuits Syst. I, Reg. Papers*, vol. 65, no. 9, pp. 3110–3121, Sep. 2018.
[15] H. Li, K. Wang, J. Fang, and Y. Tang, "Pulse density modulated ZVS full-bridge converters for wireless power transfer systems," *IEEE Trans. Power Electron.*, vol. 34, no. 1, pp. 369–377, Jan. 2019.
[16] Z. Huang, S. C. Wong, and C. K. Tse, "An inductive-power-transfer converter with high efficiency throughout battery-charging process," *IEEE Trans. Power Electron.*, vol. 34, no. 10, pp. 1245–1255, Oct. 2019.
[17] Y. G. Su, H. Y. Zhang, Z. H. Wang, A. Patrick Hu, L. Chen, and Y. Sun, "Steady-state load identification method of inductive power transfer system based on switching capacitors," *IEEE Trans. Power Electron.*, vol. 30, no. 11, pp. 6349–6355, Nov. 2015.
[18] J. Yin, D. Lin, T. Parisini, and S. Y. R. Hui, "Front-end monitoring of the mutual inductance and load resistance in a series-series compensated wireless power transfer system," *IEEE Trans. Power Electron.*, vol. 31, no. 10, pp. 7339–7352, Oct. 2016.
[19] P. Zheng, W. Lei, F. Liu, R. Li, and C. Lv, "Primary control strategy of magnetic resonant wireless power transfer based on steady-state load identification method," in *Proc. IEEE Int. Power Electron. Appl. Conf. Expo.*, Nov. 2018, pp. 1–5.
[20] Y. Yang, Y. Jiang, S. C. Tan, and S. Y. R. Hui, "A frequency-sweep based load monitoring method for weakly-coupled series-series compensated wireless power transfer systems," in *Proc. PELS Workshop Emerg. Technol., Wireless Power Transfer*, Jun. 2018, pp. 1–5.
[21] Y. Yang, S. C. Tan, and S. Y. R. Hui, "Front-end parameter monitoring method based on two-layer adaptive differential evolution for SS-compensated wireless power transfer systems," *IEEE Trans. Ind. Informat.*, vol. 15, no. 11, pp. 6101–6113, Nov. 2019.
[22] Wireless Power Consortium, "The Qi wireless power transfer system power class 0 specification Parts 1 and 2: Interface definitions," Feb. 2017. [Online]. Available: https://www.wirelesspowerconsortium.com/knowledge-base/specifications/download-the-qi-specifications.html
[23] E. Asa, K. Colak, M. Bojarski, and D. Czarkowski, "A novel phase control of semi bridgeless active rectifier for wireless power transfer applications," in *Proc. IEEE Appl. Power Electron. Conf. Expo.*, 2015, pp. 3225–3231.
[24] S. Y. R. Hui and Y. Yang, "A wireless battery charging system and method for battery charging and handshaking," US Provisional Patent Application 62/906,180, Sep. 26, 2019.

Yun Yang (Member, IEEE) received the B.S. degree in electrical engineering from Wuhan University, Wuhan, China, in 2012, and the Ph.D. degree in power electronics from the Department of Electrical and Electronic Engineering, The University of Hong Kong, Hong Kong, in 2017.

He is currently a Postdoctoral Research Fellow with the Department of Electrical and Electronic Engineering, The University of Hong Kong. He has authored/coauthored more than 25 technical papers, including ten transaction papers as the first author. His current research interests include wireless power transfer, microgrids and renewable energy, and advanced control for power electronics.

Dr. Yang was the recipient of the Outstanding Presentation Award in Applied Power Electronics Conference and Exposition 2016 and a Session Chair or technical committee member for various conferences. He is currently an Editor for Cogent Engineering.

Siew Chong Tan (Senior Member, IEEE) received the B.Eng. (hons.) and M.Eng. degrees in electrical and computer engineering from the National University of Singapore, Singapore, in 2000 and 2002, respectively, and the Ph.D. degree in electronic and information engineering from the Hong Kong Polytechnic University, Hong Kong, in 2005.

He is currently a Professor, the Associate Head, and the Director of 100 kVA Smart Grid Research Facility and Emerging Power Electronics Laboratory, Department of Electrical and Electronic Engineering, The University of Hong Kong, Hong Kong. He has coauthored a book *Sliding Mode Control of Switching Power Converters: Techniques and Implementation* (CRC, 2011).

Dr. Tan is an Associate Editor of the IEEE TRANSACTIONS ON POWER ELECTRONICS.

Shu Yuen Ron Hui (Fellow, IEEE) received the B.Sc. (hons.) degree in engineering from the University of Birmingham, Birmingham, U.K., in 1984, and a D.I.C. and Ph.D. degrees from Imperial College London, London, U.K., in 1987.

He currently holds the Philip Wong Wilson Wong Chair Professorship with the University of Hong Kong, Hong Kong, and a Chair Professorship with Imperial College London. He has published more than 470 technical papers, including more than 270 refereed journal publications. Over 60 of his patents have been adopted by industry.

Dr. Hui is an Associate Editor of the IEEE TRANSACTIONS ON POWER ELECTRONICS and Editor of the IEEE JOURNAL OF EMERGING AND SELECTED TOPICS IN POWER ELECTRONICS. His inventions on wireless charging platform technology underpin key dimensions of Qi, the world's first wireless power standard, with freedom of positioning and localized charging features for wireless charging of consumer electronics. He was the recipient of the IEEE Rudolf Chope R&D Award from the IEEE Industrial Electronics Society and the IET Achievement Medal (The Crompton Medal) in 2010, and the IEEE William E. Newell Power Electronics Award in 2015. He has been a Fellow of the Australian Academy of Technological Sciences & Engineering since 2010, the Royal Academy of Engineering, U.K. since 2016, and US National Academy of Inventors since 2018.